



# Overcoming the numerical challenges owing to rapid ductile localization

Arne Spang<sup>1</sup>, Marcel Thielmann<sup>1,2</sup>, Casper Pranger<sup>3</sup>, Albert de Montserrat<sup>4</sup>, and Ludovic Räss<sup>5</sup>

<sup>1</sup>Bayerisches Geoinstitut, Universität Bayreuth, Universitätsstraße 30, 95447 Bayreuth, Germany

<sup>2</sup>Institut für Geowissenschaften, Universität Bonn, Meckenheimer Allee 176, 53115 Bonn, Germany

<sup>3</sup>Department für Geo- und Umweltwissenschaften, Ludwig-Maximilians-Universität München, Theresienstraße 41, 80333 München, Germany

<sup>4</sup>Department of Earth Sciences, ETH Zürich, Sonneggstrasse 5, 8092 Zürich, Switzerland

<sup>5</sup>Swiss Geocomputing Centre, Faculty of Geosciences and Environment, University of Lausanne, Lausanne Switzerland

**Correspondence:** Arne Spang (arne.spang@uni-bayreuth.de)

**Abstract.** Strain localization is among the most challenging mechanical phenomena for computational Earth sciences. Accurately capturing it is difficult because strain localization initiates spontaneously, is self-accelerating, and its characteristic length and time scales are typically significantly smaller than the spatial and temporal resolutions of the model. This results in an undesirable dependence of the model behavior on numerical parameters and a large computational cost. Strain localization is most commonly associated with brittle failure, but ductile processes such as thermal runaway can also result in rapid ductile localization. Here, we present a numerical model to investigate thermal runaway, and further propose strategies to overcome the challenges associated with resolving rapid localization: (i) adaptive time stepping; (ii) adaptive rescaling; and (iii) two types of regularization. We demonstrate the effect of these strategies in one- and two-dimensional models. We rely on the accelerated pseudo-transient method to solve the governing equations and use graphics processing units to accelerate two-dimensional computations. Our adaptive time stepping strategy allows us to accurately capture spontaneous and rapid stress release during thermal runaway while reducing time steps by more than ten orders of magnitude. Adaptive rescaling further reduces rounding errors and the number of required iterations by two orders of magnitude. Viscosity regularization and gradient regularization enable us to mitigate resolution dependencies but may differently impact the physical response of the model.

## 1 Introduction

Strain localization is a critical component of deformation that can be observed on any scale and in almost any material (Poirier, 1980; Desrues et al., 2007; Antolovich and Armstrong, 2014; Weidner and Biermann, 2021). In Geodynamics, accurately modeling strain localization remains inherently challenging due to the large differences in involved scales. A model has to cover the km-scale geological setting which evolves on time scales of kyr as well as the mm-scale localized shear zone which may operate on time scales of seconds. Furthermore, the self-feeding character of strain localization usually results in a lack of a finite length and time scale (De Borst et al., 1993; Iordache and Willam, 1998; Gerolymatou et al., 2024). As a consequence, the model behavior becomes dependent on numerical parameters such as spatial and temporal resolution and fails to accurately



capture strain localization. A plate-scale model is likely to overestimate the width of a shear zone, whereas a grain-scale model might underestimate it. Another challenge in resolving spontaneous localization is the broad spectrum of values that must be covered with sufficient numerical accuracy.

25 In the Earth's lithosphere, strain localization predominantly occurs via brittle failure. However, with increasing depth and lithostatic pressure, the brittle strength of rocks increases linearly (Drucker and Prager, 1952; Byerlee, 1978), while increasing temperatures promote ductile deformation. If brittle failure were the only mechanism to localize deformation, this would suggest that highly localized deformation should be limited to less than about 100 km depth. However, the occurrence of deep earthquakes, reaching depths of about 660 km (Turner, 1922; Wadati, 1928; Leith and Sharpe, 1936), demonstrates that strong  
30 strain localization and rapid slip can also occur under conditions that favor ductile deformation.

One mechanism proposed to facilitate ductile localization is thermal runaway (Gruntfest, 1963; Ogawa, 1987). This process, illustrated in Fig. 1a, describes a feedback cycle that includes deformation, shear heating (or viscous dissipation), temperature-dependent rheology, and localization. Once deformation begins to localize within a weak inclusion embedded in a stronger matrix (Fig. 2a,b), shear heating causes the temperature in the inclusion to rise more rapidly, thereby locally reducing the  
35 viscosity and further enhancing localization. This feedback loop can result in catastrophic strength reduction, a surge in temperature, rapid stress release, and highly localized slip (e.g., Kameyama et al., 1999; Kelemen and Hirth, 2007; Thielmann et al., 2015). Thermal diffusion can stop this feedback loop if sufficient heat is transferred from the shear zone to the surrounding host rock, which prevents further increase in the viscosity contrast between the units (Braeck et al., 2009; Thielmann, 2018; Spang et al., 2024).

40 In Spang et al. (2024), we captured the dynamics of thermal runaway using a one-dimensional thermomechanical simple shear model, which predicts the temporal evolution of stress and temperature within an evolving shear zone (Fig. 1b). The model evolves through five distinct stages: (i) elastic loading, during which deviatoric stress increases linearly while temperature remains constant; (ii) steady-state viscous creep, dominated by low-temperature plasticity (LTP), where stress remains nearly constant and temperature increases steadily; (iii) thermal runaway, in which deformation localizes into a narrowing slip  
45 zone dominated by dislocation creep, leading to a significant stress drop and an exponential increase in temperature; (iv) post-runaway loading, characterized by linear stress increase as heat diffuses from the shear zone into the surrounding host rock; and (v) post-runaway creep, where stress gradually decreases as the system transitions into a stable sliding regime.

Similarly to brittle failure, the transient and nonlinear runaway phase presents several challenges that thermomechanical models must overcome to achieve an accurate numerical solution: (i) spontaneous initiation; (ii) poor nonlinear solver conver-  
50 gence; (iii) unstable solutions; and (iv) mesh-dependent results.

In this study, we present and discuss the one- and two-dimensional (1D and 2D) models we used to capture spontaneous ductile shear localization. We incorporate a visco-elastic, composite rheology and utilize the accelerated pseudo-transient (APT) method to solve the governing system of equations. We then focus on the numerical challenges associated with rapid localization and describe our strategies to overcome them: (i) adaptive time stepping; (ii) adaptive rescaling; (iii) viscosity  
55 regularization; (iv) gradient regularization; and (v) monitoring viscosity convergence. Readers interested in the application of these models are referred to Spang et al. (2024) and Spang et al. (2025a) for the 1D and 2D cases, respectively.

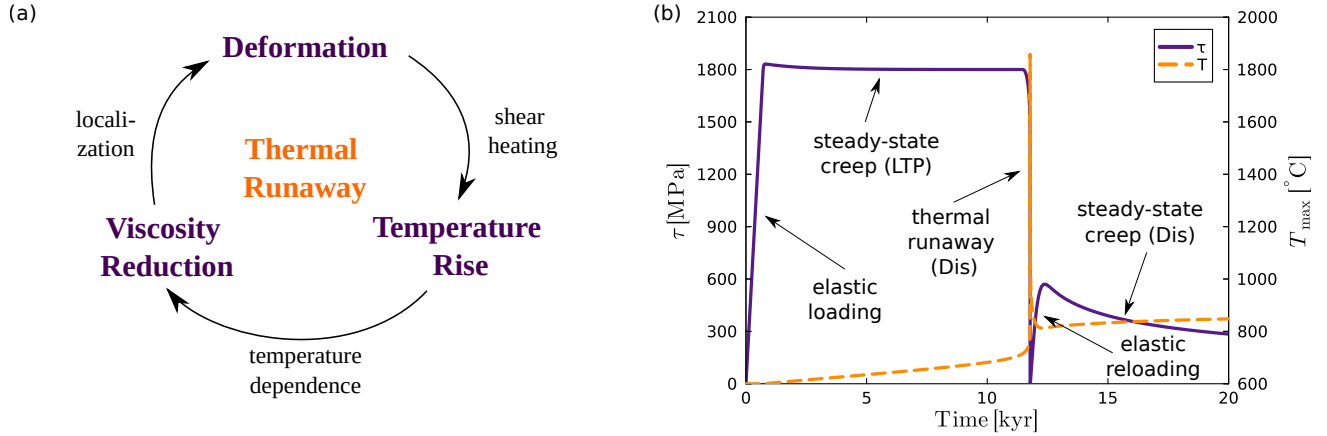


**Figure 1.** Illustration of thermal runaway. (a) Feedback cycle of processes that combine to make thermal runaway. (b) Temporal evolution of deviatoric stress (purple) and maximum temperature (orange). Arrows indicate different stages of the model evolution. LTP and Dis are short for low-temperature plasticity and dislocation creep respectively, and indicate the dominant deformation mechanism of the stages.

## 2 Methods

### 2.1 Model setup

We use models with simple shear boundary conditions and central weak inclusions to initialize localization of deformation. In 1D, the weak zone is introduced by multiplying the flow law prefactors  $A_{\text{dif}}$  and  $A_{\text{dis}}$  (see Sect. 3.2) by a weakening factor  $\omega$  which follows a Gaussian distribution with a minimum of 1 and a maximum of 2 (Fig. 2a). The full-width-half-maximum of the distribution is 200 m, and the extent of the entire model is 10 km.

The vertical and horizontal extents of the 2D model are 10 km and 60 km, respectively. The weak inclusion is an ellipse with semi-major axes of 375 m and 125 m, respectively. Within this anomaly,  $A_{\text{dif}}$  and  $A_{\text{dis}}$  are multiplied by 2, and  $\sigma_b$  is divided by 2. The different implementations of the weak inclusion are discussed in Sect. 5. The lateral boundary conditions in the 2D model are periodic (Fig. 2b).

### 2.2 Governing equations

To capture rapid ductile shear localization, we consider a system of coupled thermomechanical equations. In Sect. 2.2.1, we present the general set of equations which are valid for any number of spatial dimensions, whereas Sect. 2.2.2 outlines how the equations can be simplified for the 1D case.

#### 2.2.1 The general case

We consider the conservation of momentum, mass, and energy:

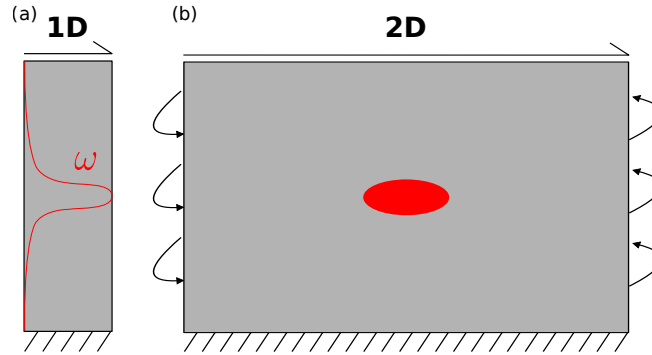


**Figure 2.** Model setups with simple shear boundary conditions. (a) 1D model. Note that the model only has a single cell in the horizontal direction. The red line indicates the distribution of the weakening factor  $\omega$ . (b) 2D model. The red ellipse indicates the weak inclusion where the weakening factor  $\omega$  is applied. Lateral boundaries are periodic. Both setups are not drawn to scale. Adapted from Spang et al. (2024) and Spang et al. (2025a).

$$\frac{\partial \tau_{ij}}{\partial x_j} - \frac{\partial P}{\partial x_i} = 0, \quad (1)$$

$$\frac{1}{\rho} \frac{\partial \rho}{\partial t} = - \frac{\partial v_i}{\partial x_i}, \quad (2)$$

$$\rho C_p \frac{\partial T}{\partial t} = \frac{\partial}{\partial x_i} \left( \lambda \frac{\partial T}{\partial x_i} \right) + \tau_{ij} \dot{\epsilon}_{ij}^{vi}, \quad (3)$$

where  $\tau_{ij}$  is the Cauchy stress deviator,  $x_i$  denotes the Cartesian coordinates,  $P$  is pressure (positive in compression),  $\rho$  is density,  $t$  is time,  $v_i$  is the velocity vector,  $C_p$  is specific heat capacity,  $T$  is temperature,  $\lambda$  is thermal conductivity, and  $\dot{\epsilon}_{ij}^{vi}$  is the viscous component of the deviatoric strain rate. For simplicity, we neglect the inertial terms, body forces (i.e. gravity), thermal expansion, as well as adiabatic and radiogenic heating. The conservation equations are augmented by constitutive

relations for bulk compressibility and Maxwell visco-elasticity:

$$\frac{1}{K_b} \frac{\partial P}{\partial t} = - \frac{\partial v_i}{\partial x_i}, \quad (4)$$

$$\dot{\epsilon}_{ij} = \dot{\epsilon}_{ij}^{el} + \dot{\epsilon}_{ij}^{vi} = \frac{1}{2G} \frac{\partial \tau_{ij}}{\partial t} + \frac{1}{2\eta} \tau_{ij}, \quad (5)$$

where  $K_b$  is the bulk modulus,  $\dot{\epsilon}_{ij}^{vi}$  is the deviatoric strain rate and  $\dot{\epsilon}_{ij}^{el}$  is its elastic component,  $G$  is the shear modulus, and  $\eta$  is the effective viscosity. The deviatoric strain rate is defined as:

$$\dot{\epsilon}_{ij} = \frac{1}{2} \left( \frac{\partial v_i}{\partial x_j} + \frac{\partial v_j}{\partial x_i} \right) - \frac{1}{3} \frac{\partial v_k}{\partial x_k} \delta_{ij}, \quad (6)$$

where  $\delta_{ij}$  is the Kronecker-Delta.



### 2.2.2 The 1D case

In the 1D configuration, the system of governing equations (1) - (6) is simplified. The spatial dimensions are reduced to the vertical  $y$ -direction. With simple shear boundary conditions, no gravity, and no thermal expansion, the divergence of velocity is inherently zero. The conservation of mass (Eq. (2)) simplifies to:

$$\frac{\partial \rho}{\partial t} = 0, \quad (7)$$

and Eq. (4) simplifies to:

$$\frac{\partial P}{\partial t} = 0. \quad (8)$$

This renders the model incompressible, with density and pressure constant in time. Furthermore, the velocity vector is reduced to its horizontal component, which simplifies Eq. (6) to:

$$\dot{\epsilon}_{xy} = \frac{1}{2} \frac{\partial v_x}{\partial y}, \quad (9)$$

with the other components of the strain rate and stress tensor equal to zero. This simplifies the conservation of momentum (Eq. (1)) to:

$$\frac{\partial \tau_{xy}}{\partial y} = 0. \quad (10)$$

## 3 Implementation

The governing equations are discretized on a staggered grid (e.g., Gerya and Yuen, 2003) and solved using a conservative finite-difference scheme in an iterative manner using the APT method (Frankel, 1950; Räss et al., 2022; Alkhimenkov and Podladchikov, 2024). The code is implemented in the Julia programming language and employs the GEOPARAMS.JL package (Kaus et al., 2023) for parameter nondimensionalization. The 2D implementation further leverages the PARALLELSTENCIL.JL package (Omlin and Räss, 2024) to automatically generate parallel kernels on both central processing unit (CPU) and graphics processing unit (GPU) devices.

### 3.1 Accelerated pseudo-transient method

In the APT approach, the conservation equations are solved at each physical time step by introducing a pseudo-time derivative for each equation and iteratively updating the primary variables  $v$ ,  $P$ , and  $T$  until the residuals drop below a given numerical tolerance. Applying this procedure to Eq. (1)-(3) yields:



$$\frac{\partial v_i}{\partial \psi} = \frac{\partial \tau_{ij}}{\partial x_j} - \frac{\partial P}{\partial x_i}, \quad (11)$$

$$\frac{\partial P}{\partial \psi} = \frac{1}{K_b} \frac{\partial P}{\partial t} + \frac{\partial v_i}{\partial x_i}, \quad (12)$$

$$\frac{\partial T}{\partial \psi} = \frac{1}{\rho C_p} \left[ \frac{\partial}{\partial x_i} \left( \lambda \frac{\partial T}{\partial x_i} \right) + \tau_{ij} \dot{\epsilon}_{ij}^{vi} \right] - \frac{\partial T}{\partial t}, \quad (13)$$

where  $\partial/\partial\psi$  denotes the pseudo-time derivative. During each pseudo-time iteration, each primary variable is incremented  
115 proportionally to the sum of the current residual and the previous increment (Duretz et al., 2019):

$$\Delta_\gamma = \left[ \frac{\partial \gamma}{\partial \psi} + \left( 1 - \frac{1}{\zeta_\gamma} \right) \Delta_\gamma^{\text{prev}} \right] \Delta \psi_\gamma, \quad (14)$$

where  $\gamma$  represents one of the primary variables  $v$ ,  $P$ , or  $T$ ,  $\Delta_\gamma$  is the current increment of the respective variable,  $\Delta_\gamma^{\text{prev}}$  is the increment from the previous iteration,  $\zeta_\gamma$  is the damping parameter ( $> 1$ ).  $\Delta \psi_\gamma$  is the size of the pseudo-time step given by:

$$\Delta \psi_{v_i} = \frac{\Delta x_i}{f_v \eta}, \quad (15)$$

$$120 \quad \Delta \psi_P = \frac{f_P \eta}{\max(\text{nc}_i)}, \quad (16)$$

$$\Delta \psi_T = \min \left( \frac{\min(\Delta x_i)^2}{2 n_{\text{dim}} \kappa}, \frac{\Delta t}{2} \right), \quad (17)$$

where  $\Delta x_i$  is the grid spacing,  $f_v$  and  $f_P$  are factors,  $\text{nc}_i$  is the number of cells in each dimension,  $n_{\text{dim}}$  is the number of dimensions,  $\kappa = \lambda/(\rho C_p)$  and  $\Delta t$  is the physical time step.

The left hand side terms in Eq. (11) - (13) are equivalent to the residuals of the conservation equations. Once all of them  
125 are smaller than a given numerical tolerance of  $10^{-6}$  after normalization, the solution is converged and is equivalent to a fully implicit, backward Euler solution with converged nonlinearities.

### 3.2 Rheology

Viscous deformation is a combination of diffusion creep, dislocation creep, and low-temperature plasticity. We follow the approach of Maxwell (Maxwell, 1867; Jóźwiak et al., 2015) and consider all viscous mechanisms in series, which implies that  
130 deformation is dominated by the weakest one and that strain rate components are added:

$$\dot{\epsilon}_{\text{II}}^{\text{vi}} = \dot{\epsilon}_{\text{II}}^{\text{dif}} + \dot{\epsilon}_{\text{II}}^{\text{dis}} + \dot{\epsilon}_{\text{II}}^{\text{LTP}}, \quad (18)$$

where the superscripts dif, dis and LTP denote diffusion creep, dislocation creep, and low-temperature plasticity, respectively. The subscript II denotes the square root of the second invariant of an arbitrary second-order tensor  $C$ :



$$C_{II} = \sqrt{\frac{1}{2} C_{ij} C_{ij}} . \quad (19)$$

135 As a consequence of the Maxwell approach in Eq. (18), the effective viscosity  $\eta$  can be expressed as:

$$\eta = \left( \frac{1}{\eta_{\text{dif}}} + \frac{1}{\eta_{\text{dis}}} + \frac{1}{\eta_{\text{LTP}}} \right)^{-1} , \quad (20)$$

where

$$\eta_{\text{dif}} = \frac{1}{2} (A_{\text{dif}})^{-1} d^m \exp \left( \frac{E_{\text{dif}}}{RT} \right) , \quad (21)$$

$$\eta_{\text{dis}} = \frac{1}{2} (A_{\text{dis}})^{-\frac{1}{n}} (\dot{\epsilon}_{\text{II}}^{\text{dis}})^{\frac{1}{n}-1} \exp \left( \frac{E_{\text{dis}}}{nRT} \right) , \quad (22)$$

$$140 \quad \eta_{\text{LTP}} = \frac{\tau_{\text{LTP}}}{2 \dot{\epsilon}_{\text{II}}^{\text{LTP}}} . \quad (23)$$

$A$  is a prefactor,  $E$  is the activation enthalpy,  $d$  is grain size,  $m$  is the grain size exponent of diffusion creep,  $R$  is the universal gas constant, and  $n$  is the powerlaw exponent of dislocation creep. The LTP-stress  $\tau_{\text{LTP}}$  is given by:

$$\tau_{\text{LTP}} = \frac{RT}{E_{\text{LTP}}} \sigma_{\text{res}} \sinh^{-1} \left[ \frac{\dot{\epsilon}_{\text{II}}^{\text{LTP}}}{A_{\text{LTP}}} \exp \left( \frac{E_{\text{LTP}}}{RT} \right) \right] + \sigma_{\text{b}} , \quad (24)$$

$$\sigma_{\text{res}} = \sigma_{\text{L}} + \frac{\sigma_{\text{K}}}{\sqrt{d}} , \quad (25)$$

145 where  $\sigma_{\text{b}}$ ,  $\sigma_{\text{L}}$  and  $\sigma_{\text{K}}$  are material constants (Hansen et al., 2019). Given the nonlinear nature of dislocation creep and low-temperature plasticity, the strain rate partitioning (Eq. (18)) can not be solved analytically, but requires an iterative approach. It can be updated and solved alongside the conservation equations (11) - (13). To stabilize the rheology solver, we use a relaxation approach for the viscosity updates of each mechanism during the pseudo-transient (PT) iterations:

$$\eta_i^{\text{it}} = \exp \left[ (1 - \eta_{\text{rel}}) \log(\eta_i^{\text{it}-1}) + \eta_{\text{rel}} \log(\eta_i^{\text{t}}) \right] , \quad (26)$$

150 where the superscript it denotes the iteration count,  $\eta_{\text{rel}} < 1$  is the relaxation factor (Duretz et al., 2019), and  $\eta_i^{\text{t}}$  is the target viscosity (i.e. the new viscosity without relaxation). We discuss our strategy for solving the strain rate partitioning in Appendix A and Fig. A1.

### 3.3 Density

The density in the model is a function of the reference density  $\rho_0 = 3300 \text{ kg m}^{-3}$ , the pressure  $P$ , the Poisson's ratio  $\nu = 0.25$ ,  
155 and the bulk modulus  $K_{\text{b}}$ :



$$\rho = \rho_0 \exp\left(\frac{P}{K_b}\right), \quad (27)$$

$$K_b = \frac{2G(1+\nu)}{3(1-2\nu)}. \quad (28)$$

### 3.4 Spatial discretization

We employ an irregularly spaced grid in which the vertical cell size is smallest in the center of the model. In the 1D models, the central quarter of the grid consists of uniformly sized cells, while spacing increases linearly towards the model boundaries. The outermost cells are approximately 125 times larger than those at the center, allowing for maximum resolution in the region where thermal runaway is expected to occur. This is common practice when investigating thermal runaway (e.g., Thielmann et al., 2015). Material properties and most field variables are defined at cell centers, whereas velocity and heat flux are located at cell edges (Fig. A2a).

In 2D, the grid refinement is limited to a factor of 2 to avoid convergence issues arising from large cell aspect ratios. Material properties, temperature, pressure, viscous dissipation, and normal stress components are defined at cell centers. Velocity and heat flux are defined on cell edges, while shear stress components are located at cell corners (Fig. A2b). Unless stated otherwise, the material parameters used in all models are listed in Table 1.

### 3.5 Regularization

To stabilize the model during thermal runaway and mitigate mesh dependency, we test two regularization strategies: (i) viscosity regularization and (ii) gradient regularization. Both approaches aim to limit maximum strain rates and prevent viscosities from dropping below a critical threshold. We note that alternative regularization strategies have also been proposed in the literature (e.g., Duretz et al., 2023; Goudarzi et al., 2023; Gerolymatou et al., 2024).

#### 3.5.1 Viscosity regularization

Viscosity regularization imposes a direct lower bound on viscosity, effectively stopping the self-softening behavior of thermal runaway once this threshold is reached. To implement this, we modify equation (20) as follows:

$$\eta = \left( \frac{1}{\eta_{\text{dif}}} + \frac{1}{\eta_{\text{dis}}} + \frac{1}{\eta_{\text{LTP}}} \right)^{-1} + \eta_{\text{reg}}, \quad (29)$$

where  $\eta_{\text{reg}}$  is the regularization viscosity. This approach has been previously applied to regularize brittle plasticity (Duretz et al., 2020; Jacquey and Cacace, 2020; Kiss et al., 2023; Alkhimenkov et al., 2024) and rate-and-state friction models (Pranger et al., 2022; Goudarzi et al., 2023). Our rheological model is illustrated in Fig. A1.





**Table 1.** Material parameters for the reference model. Bracketed superscripts denote the sources of the flow law parameters which are given at the bottom of the table.

Parameter	Unit	Value
$T_0$	[°C]	600
$P_0$	[GPa]	10
$\dot{\epsilon}_{bg}$	[s <sup>-1</sup> ]	$5 \times 10^{-13}$
$\rho_0$	[kg m <sup>-3</sup> ]	3300
$d$	[μm]	100
$\eta_{reg}$	[Pa · s]	$10^{15}$
$G$	[GPa]	80
$m$		3 <sup>[1]</sup>
$A_{dif}$	[μm <sup>m</sup> MPa <sup>-1</sup> s <sup>-1</sup> ]	$1.5 \times 10^9$ <sup>[1]</sup>
$E_{dif}$	[kJ mol <sup>-1</sup> ]	375 <sup>[1]</sup>
$n$		3.5 <sup>[1]</sup>
$A_{dis}$	[MPa <sup>-n</sup> s <sup>-1</sup> ]	$1.1 \times 10^5$ <sup>[1]</sup>
$E_{dis}$	[kJ mol <sup>-1</sup> ]	530 <sup>[1]</sup>
$A_{LTP}$	[s <sup>-1</sup> ]	$5 \times 10^{20}$ <sup>[2]</sup>
$E_{LTP}$	[kJ mol <sup>-1</sup> ]	550 <sup>[2]</sup>
$\sigma_L$	[GPa]	3.1 <sup>[2]</sup>
$\sigma_K$	[GPa μm <sup>0.5</sup> ]	3.2 <sup>[2]</sup>
$\sigma_b$	[GPa]	1.8 <sup>[2]</sup>
$C_p$	[J kg <sup>-1</sup> K <sup>-1</sup> ]	1000
$\lambda$	[J s <sup>-1</sup> m <sup>-1</sup> K <sup>-1</sup> ]	3
$\nu$		0.25

<sup>1</sup>Hirth and Kohlstedt (2003), <sup>2</sup>Hansen et al. (2019).

### 3.5.2 Gradient regularization

In gradient regularization, the viscous dissipation is distributed over a broader area, which limits localized temperature increase, viscosity reduction, and strain localization. This is achieved by introducing a diffusion term to the shear heating component of the conservation of energy (Eq. (3)):

$$185 \quad \rho C_p \frac{\partial T}{\partial t} = \frac{\partial}{\partial x_i} \left( \lambda \frac{\partial T}{\partial x_i} \right) + \tau_{ij} \left( \dot{\epsilon}_{ij}^{vi} + \lambda_{reg}^2 \frac{\partial^2 \dot{\epsilon}_{ij}^{vi}}{\partial x_i^2} \right), \quad (30)$$

where  $\lambda_{reg}$  is a regularizing diffusion length scale. This approach has also been employed in the regularization of rate-and-state friction models (Sleep, 1997; Pranger et al., 2022) and tested in the context of brittle faulting (De Borst and Mühlhaus, 1992; Duretz et al., 2023).



## 4 Challenges

190 To illustrate the challenges associated with rapid strain localization and the strategies we employ to address them, we use 1D models for conciseness. As similar challenges arise in 2D models, all mitigation strategies discussed here are also implemented in our 2D simulations, which are discussed in Sect. 5. The primary challenges include: (i) selecting appropriate time steps to accurately capture the runaway phase; (ii) avoiding round-off errors caused by abrupt shifts in the model's characteristic time scales; (iii) maintaining solver stability during runaway; and (iv) minimizing resolution dependence.

### 195 4.1 Adaptive time stepping

Outside the runaway phase, time steps ranging from tens to thousands of years are sufficient. However, resolving the thermal runaway phase requires time steps on the order of milliseconds. While large time steps may adequately capture the long-term stress evolution, they fail to resolve the transient dynamics leading up to runaway (Fig. 3a). In particular, they significantly underestimate temperature increase and slip velocity.

200 As the spontaneous onset of runaway cannot be predicted a priori, an adaptive time-stepping scheme is critical. Identifying suitable time steps is a well-known challenge in scientific computing, with numerous solutions proposed in the literature (Ropp et al., 2004). Given that stress and temperature exhibit the most rapid changes during runaway, we constrain time steps by limiting the maximum allowable increment in these two quantities ( $\Delta\tau$ ,  $\Delta T$ ). Similar strategies are employed in earthquake modeling studies (Herrendörfer et al., 2018; Dal Zilio et al., 2022; Pranger et al., 2022).

205 We evaluate three methods for implementing adaptive time stepping. In all cases, we define threshold values of  $\Delta\tau_{\max} = 50 \text{ MPa}$  and  $\Delta T_{\max} = 5 \text{ K}$ .

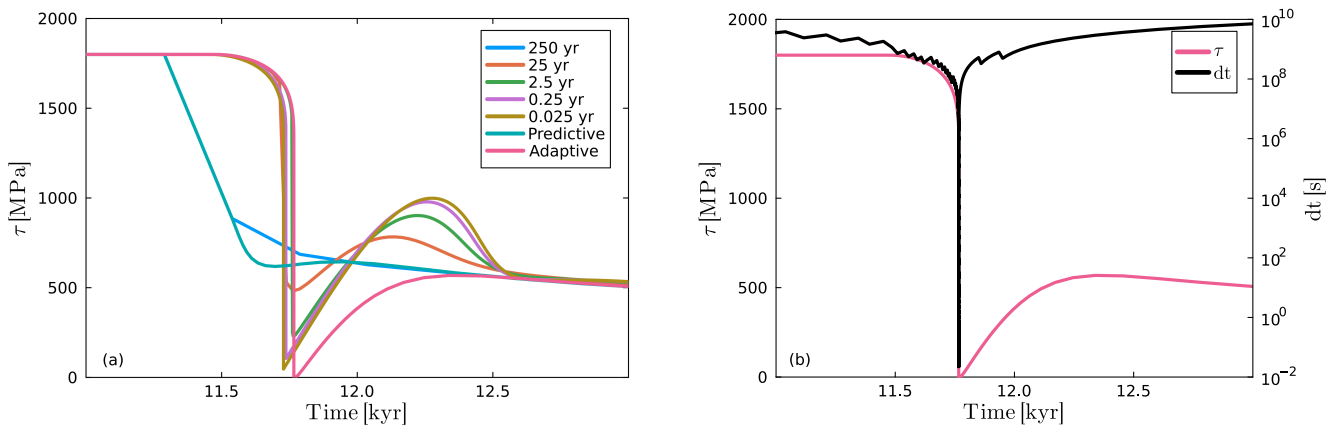


**Figure 3.** Effects of adaptive time stepping. (a) Temporal stress evolution as a function of fixed time steps of different size in comparison to linear-predictive (Sect. 4.1.1) and restarting-adaptive (Sect. 4.1.3) time stepping. (b) Temporal evolution of stress and time step, using the restarting-adaptive method.  $\eta_{\text{reg}} = 10^9 \text{ Pa}\cdot\text{s}$ .



#### 4.1.1 Linear-predictive

For the linear-predictive scheme, we assume that the rates of change of stress  $\tau$  and temperature  $T$  do not increase significantly in the subsequent time step. Based on this assumption, the new time step can be determined by scaling the previous time step according to the changes in  $\tau$  and  $T$  during it:

$$\Delta t^{nt} = \Delta t^{nt-1} \min \left( \frac{\Delta T_{\max}}{\Delta T^{nt-1}}, \frac{\Delta \tau_{\max}}{\Delta \tau^{nt-1}} \right), \quad (31)$$

where  $\Delta t^{nt}$  is the upcoming time step,  $\Delta t^{nt-1}$  is the previous time step,  $\Delta T^{nt-1}$  is the maximum temperature change during the previous step, and  $\Delta \tau^{nt-1}$  is the stress change (which is spatially uniform in the 1D domain).

If the actual rates of change in  $\tau$  and  $T$  increase, the resulting  $\Delta \tau$  and/or  $\Delta T$  may exceed their respective thresholds  $\Delta \tau_{\max}$  and  $\Delta T_{\max}$ . This causes the subsequent time step to be shorter. However, due to the highly nonlinear nature of thermal runaway, this predictive scheme may be inadequate, failing to decrease the time step fast enough once localization and stress release begin (Fig. 3a).

#### 4.1.2 Iteration-adaptive

In the iteration-adaptive scheme, we also use Eq. (31) to predict the new time step. However, instead of applying it only once at the beginning of a physical time step, we dynamically adjust the time step during every iteration of the APT solver. This approach enables rapid reduction of the time step by several orders of magnitude within a single physical time step, while still adhering to the constraints set by  $\Delta \tau_{\max}$  and  $\Delta T_{\max}$ . However, as the elastic component of the strain rate is time step-dependent (Eq. (5)), adapting the time step during PT iterations can lead to unstable behavior where the residuals oscillate and fail to converge.

#### 4.1.3 Restarting-adaptive

In the restarting-adaptive scheme, we rely on Eq. (31) to evaluate the appropriate time step during PT iterations. However, unlike the iteration-adaptive approach, the time step is not reduced within the PT iterations. Instead, if Eq. (31) indicates that the current time step is too large, the entire physical time step is restarted with a reduced (by a factor of 2) step size. To facilitate this, all relevant fields – stress, temperature, pressure, density, viscosity, and velocity – are saved at the start of each new time step. If a restart is triggered, these values are restored, and the time step is recalculated.

Multiple restarts per time step are possible and often necessary during the onset of thermal runaway. This strategy is effective in ensuring solver stability while rapidly adapting the time step. Its primary drawback is that some redundant computations occur during restarts. However, the redundancy is generally small compared to the overall computations (and iterations) required to solve each time step.

To avoid excessive time step increases, we also cap time step growth to 25% of the previous value when  $\Delta t$  is predicted to increase. Figure 3b illustrates the performance of this method. The time step initially remains on the order of hundreds of



years during the steady-state creep phase, drops by approximately two orders of magnitude as stress begins to relax, and then decreases by another ten orders of magnitude during the onset of thermal runaway. In the elastic reloading phase,  $\Delta t$  quickly recovers to hundreds of years as both stress and temperature evolve more slowly.

## 240 4.2 Adaptive rescaling

Numerical solvers commonly use internal scaling to center quantities around 1 which minimizes round-off errors due to numerical precision. To do so, a set of characteristic scales is created, and all dimensional quantities are divided by an appropriate combination of these scales. As an example, a geodynamic model focused on plate-scale deformation might use a characteristic time scale of  $t_c = 10^{12}$  s and a characteristic stress of  $\tau_c = 10^8$  Pa which combine to a characteristic viscosity of  $10^{20}$  Pa · s.

245 This means a time step of 100 years would internally be:

$$\Delta t_{ND} = \frac{\Delta t}{t_c} \approx 0.003156. \quad (32)$$

This becomes problematic once adaptive time stepping reduces the dimensional time step to one second, as this is equivalent to  $10^{-12}$  after scaling. To prevent round-off errors in this case, we decrease  $t_c$  by one order of magnitude every time the nondimensional time step drops below a certain value (e.g.,  $10^{-9}$ ). Changing the characteristic time scale does not only impact  
250 the nondimensional time step but all quantities which carry units of seconds such as strain rates, velocities, and viscosities. All of these have to be rescaled together. This is convenient for viscosities as they also decrease significantly during runaway. It is also beneficial for velocities and strain rates as they increase during runaway and decreasing  $t_c$  increases the characteristic velocity and strain rate.

In Fig. 4, we demonstrate how rescaling facilitates convergence and reduces the number of iterations by orders of magnitude  
255 for a model that takes time steps as low as  $25 \mu\text{s}$ . Without rescaling, the model requires about  $2 \times 10^9$  iterations in total to solve, the majority of them during thermal runaway. Rescaling properties with time scales in their units as soon as the nondimensional time step  $\Delta t_{ND}$  falls below  $10^{-14}$  reduces the number of iterations by one order of magnitude. Rescaling at  $\Delta t_{ND} < 10^{-12}$  lowers the total number of iterations by another order of magnitude, and only half of them are used during the runaway. Further reduction of the critical  $\Delta t_{ND}$  has only negligible effects (Fig. 4).

## 260 4.3 Regularization

During thermal runaway, the viscosity within the shear zone decreases dramatically due to the temperature increase. Large contrasts in material properties are generally challenging for numerical solvers (e.g., Gerya, 2019), especially for iterative approaches which rely on local conditioning. Even if the solver converges, shear zones often thin to the width of one grid cell. In this case, the mechanical behavior of the model is governed by the numerical resolution instead of the material parameters  
265 (De Borst et al., 1993; Iordache and Willam, 1998; Jacquey et al., 2021). To alleviate this issue, we test two regularization methods: a viscosity regularization (see Sect. 3.5.1) and a gradient regularization (see Sect. 3.5.2). To quantify the impact of

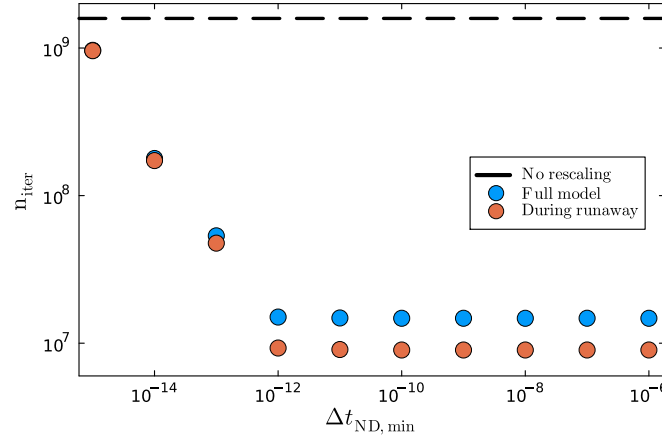


**Figure 4.** Effects of adaptive rescaling. Sum of iterations for full model (blue) and during runaway (orange) as a function of the minimum allowed  $\Delta t_{ND}$  before rescaling is used to increase it. The dashed black line shows the number of iterations without any rescaling. Note that the models with  $\Delta t_{ND,min} = 10^{-15}$  and no rescaling have many non-converged time steps. All models have identical results in terms of stress, temperature and velocity.  $\eta_{reg} = 10^6$  Pa·s.

these regularizations, we run 60 simulations in total in which we vary between five different numerical resolutions, with six different viscosity regularization values  $\eta_{reg}$ , and six different gradient regularization values  $\lambda_{reg}$ .

#### 4.3.1 Viscosity regularization

270 Applying viscosity regularization renders primary model diagnostic parameters – maximum velocity  $v_{max}$ , maximum temperature  $T_{max}$  and shear zone width  $d_{sz}$  – resolution independent (Fig. 5a,b,c). Instead, these quantities exhibit a strong, exponential dependence on the regularization viscosity  $\eta_{reg}$ . For  $\eta_{reg} \geq 10^{12}$  Pa·s, these quantities remain nearly identical across all tested grid resolutions, ranging from 63 to 1023 cells (corresponding to minimum cell sizes between 2 m and 0.125 m). At  $\eta_{reg} = 10^{12}$  Pa·s, the shear zone localizes to a single grid cell in the coarsest model (63 cells; blue curve in Fig. 5). For lower values of  $\eta_{reg}$ ,  
 275 results from this low-resolution model begin to diverge from those of finer grids. As  $\eta_{reg}$  is further reduced, this divergence propagates to higher-resolution models, following the same pattern.

Once a model localizes deformation to a single grid cell, both  $d_{sz}$  and  $T_{max}$  plateau and cease to vary with decreasing  $\eta_{reg}$  (Fig. 5b,c). In contrast,  $v_{max}$  continues to increase as  $\eta_{reg}$  decreases, but it also slowly diverges from models that are still resolved.

280 The total number of PT iterations  $n_{iter}$ , normalized by grid resolution, decreases with increasing  $\eta_{reg}$ , reflecting the fact that a more strongly regularized runaway is numerically easier to solve (Fig. 5d). Higher-resolution models exhibit slightly more efficient convergence compared to lower-resolution counterparts.

The temporal evolution of deviatoric stress remains largely unaffected by variations in  $\eta_{reg}$ . For  $\eta_{reg} \leq 10^{15}$  Pa·s, the models consistently exhibit rapid and complete stress relaxation. In contrast,  $\eta_{reg} = 10^{18}$  Pa·s leads to slower and incomplete relaxation



285 (inset in Fig. 5a). This trend is observed across all resolutions. Similar effects of viscosity regularization have been reported by Spang et al. (2024).

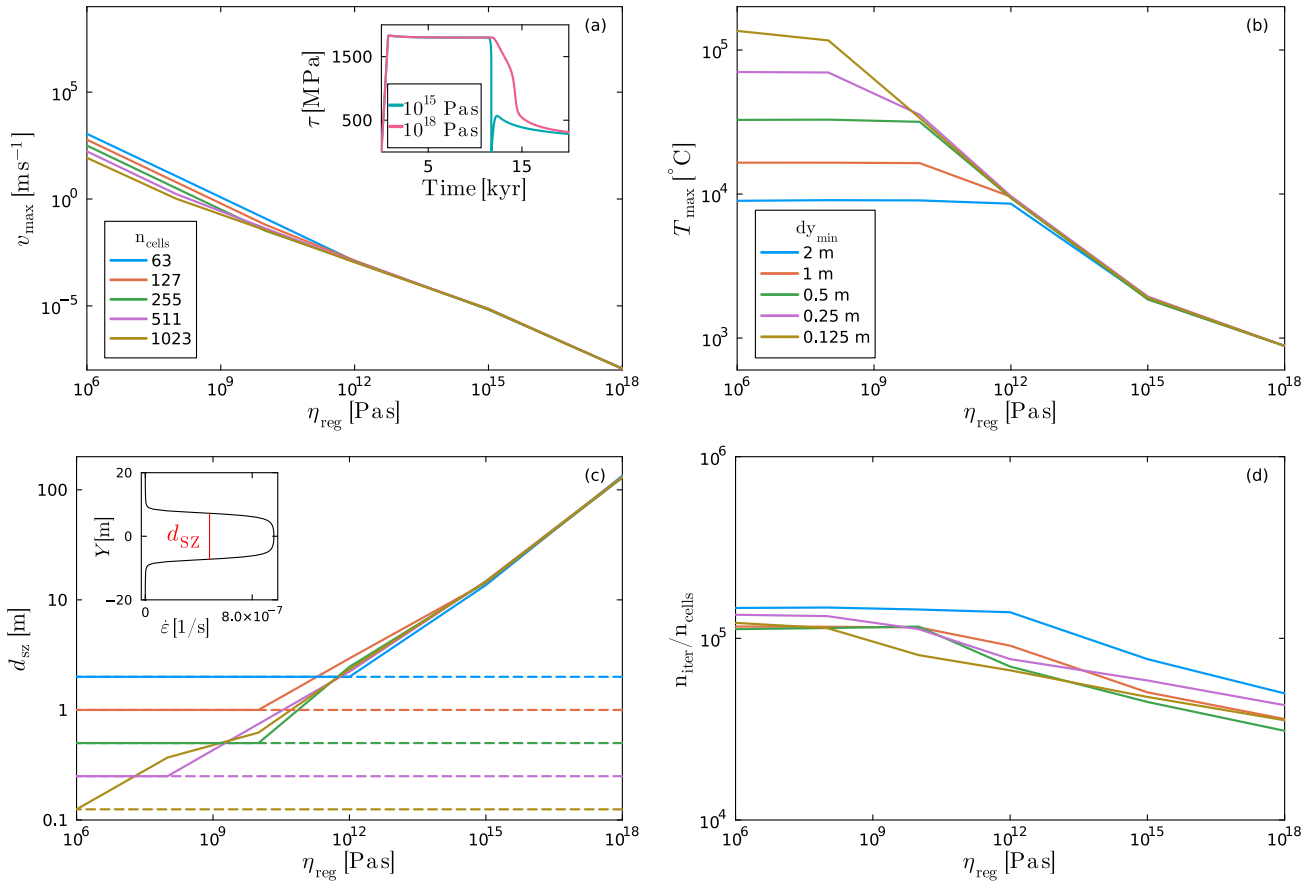


**Figure 5.** Effect of viscosity regularization. Colors correspond to resolution and all axes are logarithmic. (a) Maximum velocity. (b) Maximum temperature. (c) Shear zone width (full-width-half-maximum of strain rate peak, see inset). Dashed lines indicate size of one cell for each resolution. (d) Total number of iterations divided by number of cells. Inset in (a) shows stress evolution for 255 cells and the two largest regularization viscosities. All models with lower  $\eta_{\text{reg}}$  are indistinguishable from the example with  $\eta_{\text{reg}} = 10^{15}$  Pa·s.

### 4.3.2 Gradient regularization

As in the viscosity regularization case, applying gradient regularization renders primary model diagnostic parameters – maximum velocity  $v_{\text{max}}$ , maximum temperature  $T_{\text{max}}$  and shear zone width  $d_{\text{sz}}$  – resolution independent (Fig. 6a,b,c). Instead, these quantities exhibit a strong, exponential dependence on the regularization diffusion length scale  $\lambda_{\text{reg}}$ . While minor discrepancies persist between different resolutions, they are negligible compared to the variations induced by changes in  $\lambda_{\text{reg}}$ .



One exception is the coarsest model (63 grid cells) with  $\lambda_{\text{reg}} = 1$  m, which slightly overestimates both  $v_{\text{max}}$  and  $T_{\text{max}}$ . In this case, the shear zone has localized to a single grid cell (Fig. 6c).

Across the tested range of  $\lambda_{\text{reg}}$  (1 – 32 m),  $v_{\text{max}}$  spans from  $10^{-7}$  and  $10^7 \text{ m s}^{-1}$ ,  $T_{\text{max}}$  ranges between 800 and 4000 °C, and  $d_{\text{sz}}$  varies from approximately 3 to 100 m. Somewhat counterintuitively, larger values of  $\lambda_{\text{reg}}$  – which prevent extreme localization resulting in a more attenuated runaway – require more PT iterations resulting in larger solution time (Fig. 6d). Moreover, the number of iterations per grid cell increases with numerical resolution. Models with 511 grid cells and  $\lambda_{\text{reg}} > 8$  m, as well as 1023-cell models with  $\lambda_{\text{reg}} > 2$  m did not complete in one day and are not shown in Fig. 6. We discuss the reasons for this in Sect. 4.3.3.

For  $\lambda_{\text{reg}} \leq 8$  m, stresses relax rapidly and nearly completely. In contrast, for  $\lambda_{\text{reg}} > 8$  m, residual stresses of several hundred MPa remain at the end of the thermal runaway phase (inset in Fig. 6a).

### 4.3.3 Comparison

Both regularization strategies – viscosity and gradient regularization – achieve the same overarching goal: they effectively attenuate thermal runaway, ensure numerical stability, and provide control over the degree of strain localization. By doing so, they eliminate the dependence of diagnostic parameters on spatial resolution, making quantities such as  $v_{\text{max}}$ ,  $T_{\text{max}}$ , and  $d_{\text{sz}}$  primarily functions of  $\eta_{\text{reg}}$  or  $\lambda_{\text{reg}}$  instead. This control breaks down when the shear zone narrows to a single grid cell. At that point, regularization can no longer constrain the degree of localization, and resolution-dependent artifacts reappear.

A direct, quantitative comparison between the two methods is not straightforward, as there is no known equivalence between specific values of  $\eta_{\text{reg}}$  and  $\lambda_{\text{reg}}$ . Nevertheless, a qualitative comparison of Fig. 5 and 6 reveals distinct differences. Gradient regularization allows significantly larger  $v_{\text{max}}$  – spanning orders of magnitude beyond values observed with viscosity regularization. However,  $T_{\text{max}}$  is approximately two orders of magnitude lower when gradient regularization is employed. Although both approaches produce similar shear zone widths when considering largest regularization values, the viscosity-regularized models generate up to an order of magnitude narrower shear zones for the smallest considered regularization values. These differences stem from the fundamentally different ways the two methods constrain localization.

Viscosity regularization allows for the full release of stored elastic energy within the shear zone during stress relaxation, leading to extreme peak temperatures of up to  $10^5$  °C. However, by introducing a lower bound on viscosity, it limits the extent to which this heating can impact the rheology and weaken the material. As deformation is tightly coupled to rheology, this constraint also limits maximum slip velocities. In contrast, gradient regularization distributes the released energy across a broader region, leading to lower peak temperatures and wider shear zones. Because this method does not impose an explicit lower viscosity bound, extreme deformation rates can still occur.

The computational cost of the two methods also differs significantly, as illustrated by the normalized number of PT iterations in Fig. 5d and 6d. At low resolutions and with less pronounced regularization (low  $\eta_{\text{reg}}$  and  $\lambda_{\text{reg}}$ ), both methods perform similarly. However, as  $\eta_{\text{reg}}$  or  $\lambda_{\text{reg}}$  increase, viscosity regularization becomes more efficient, requiring fewer PT iterations. Conversely, gradient regularization becomes increasingly expensive. Larger values of  $\lambda_{\text{reg}}$  allow for faster diffusion of dissipative work, effectively reducing the maximum allowed physical time steps.

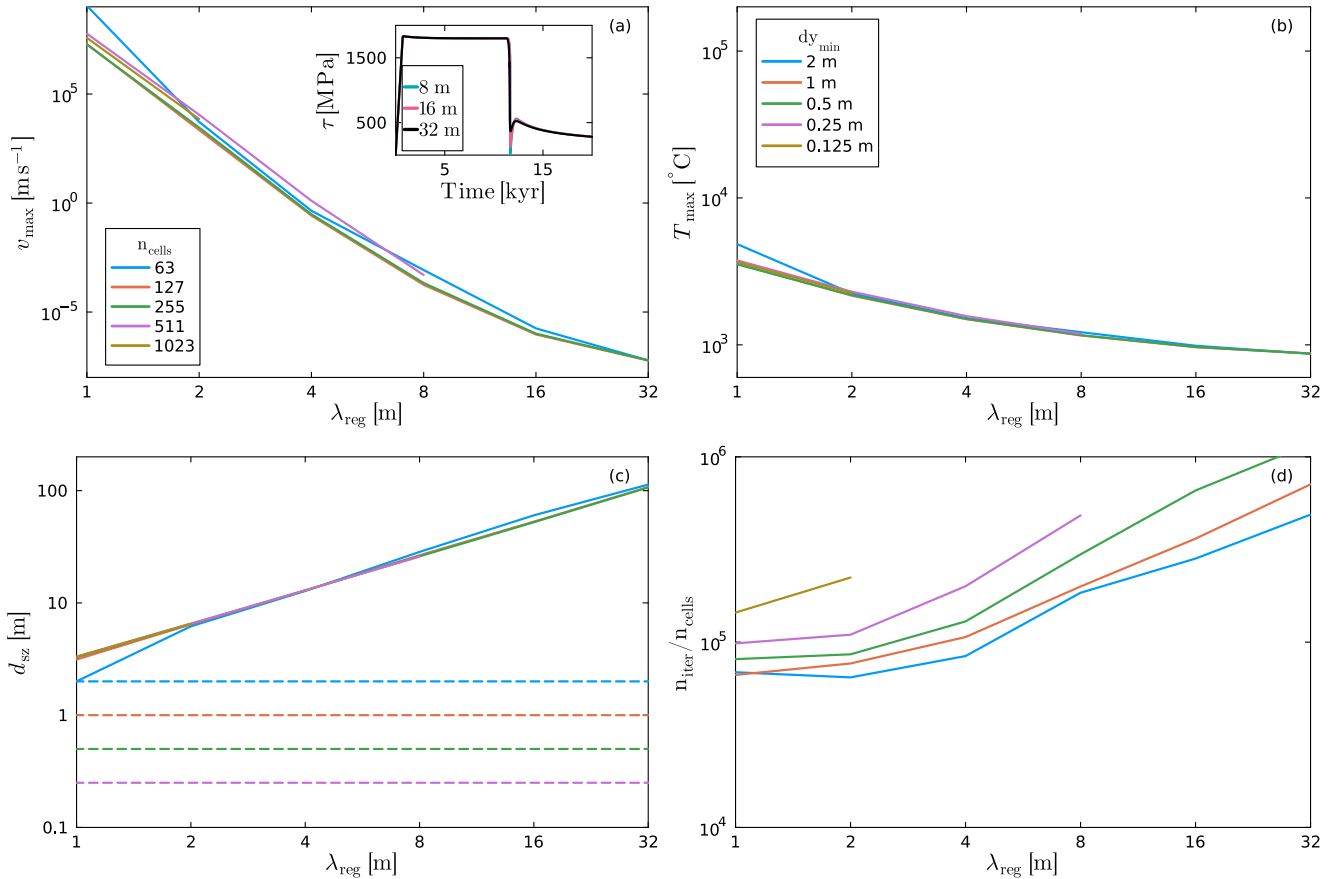


**Figure 6.** Effect of gradient regularization. Colors correspond to resolution and all axes are logarithmic. High λ<sub>reg</sub> models with 511 cells and most models with 1023 cells were excluded as they took more than one day to complete. (a) Maximum velocity. (b) Maximum temperature. (c) Shear zone width (see inset in Fig. 5c for explanation). Dashed lines indicate size of one cell for each resolution. (d) Total number of iterations divided by number of cells. Inset in (a) shows stress evolution for 255 cells and three values of λ<sub>reg</sub>. All models with lower λ<sub>reg</sub> are indistinguishable from the example with λ<sub>reg</sub> = 8 m.

Resolution scaling further differentiates the two methods. For viscosity regularization, the number of iterations per cell remains nearly constant with increasing resolution. In contrast, this ratio grows with resolution when gradient regularization is employed, making the latter increasingly impractical for high-resolution simulations. The scaling of diffusive processes is a known challenge in computational geodynamics (e.g., Räss et al., 2022).

#### 330 4.4 Converging viscosity

During the elastic loading phase, the model typically converges within a few (< 100) PT iterations. While such fast convergence is computationally efficient, it introduces challenges when using the viscosity relaxation method (Eq. (26)). In this approach,





the viscosity is incrementally updated in each iteration using a relaxation factor, commonly  $\eta_{\text{rel}} = 0.01$ , meaning that only 1% of the computed viscosity update is applied per iteration. Although this under-relaxation stabilizes the solver, it can hinder convergence of the viscosity field for a low PT iteration count.

Figure 7b shows that after 100 iterations, the viscosity update has only progressed about halfway towards its target value. Converging viscosity relaxation (i.e., reaching the updated steady-state value) typically requires around 500 iterations for  $\eta_{\text{rel}} = 0.01$ . Failing to accurately resolve viscosity relaxation may become problematic near the onset of LTP creep, where  $\eta_{\text{LTP}}$  drops rapidly as stress approaches the yield threshold  $\tau_{\text{LTP}}$ .

The behavior of LTP is similar to perfect plasticity due to brittle deformation. It remains inactive below a critical stress, but accommodates all deformation that would otherwise increase stress beyond this threshold. If  $\eta_{\text{LTP}}$  and the associated strain rate partitioning are not updated fast enough, stresses can significantly exceed  $\tau_{\text{LTP}}$ , requiring corrective adjustments in subsequent time steps (Fig. 7a). This not only leads to an incorrect stress evolution, but can also trigger spurious slip events that would not occur under properly updated stress conditions.

To mitigate this issue, we monitor the convergence between the viscosity  $\eta$  and the target viscosity  $\eta^t$  (Eq. 26). Only when the residuals of the conservation equations (Sect. 3.1), the residual of viscosity, and the residual of strain rate partitioning (Appendix A) are converged, we accept the solution. This ensures that both rheological and mechanical responses are correctly captured during the elastic-to-LTP transition (Fig. 7a).

The stress overshoot for insufficient viscosity convergence is more prominent when the steady-state stresses of diffusion and dislocation creep are large. For the model in Fig. 7a, we increased  $E_{\text{dif}}$  and  $E_{\text{dis}}$  to 435 and 670 kJ mol<sup>-1</sup>, respectively, which is equivalent to considering the pressure dependence of the rheology (Hirth and Kohlstedt, 2003) and 10 GPa of background pressure (Table 1).

## 5 The 2D implementation

All of the previously mentioned features are also implemented in the 2D version of the model. We consider a configuration with a homogeneous host rock containing a weak inclusion to perturb the stress field and initiate localization (Fig. 2b). In Fig. 8, we show the temporal evolution of such a 2D simulation, using the same parameters as the 1D reference model and a regularization viscosity of  $\eta_{\text{reg}} = 10^{12}$  Pa·s.

The 2D model undergoes the same stages as in 1D. An initial, homogeneous elastic loading stage is followed by the onset of LTP at the tips of the inclusion. Subsequently, a shear zone forms and starts to develop horizontally across the domain (Fig. 8a, b), before deformation becomes more localized near the anomaly tips (Fig. 8c). Thermal runaway initiates here and then propagates horizontally across the domain (Fig. 8d-f), creating a rupture front marked by a sharp stress gradient (Fig. 8, left column) and a peak in horizontal velocity (Fig. 8, central column). The simulation is stopped once the stress is fully released. Here, we focus on the numerical behavior of the 2D model; for a detailed discussion of the physical implications, refer to Spang et al. (2025a).

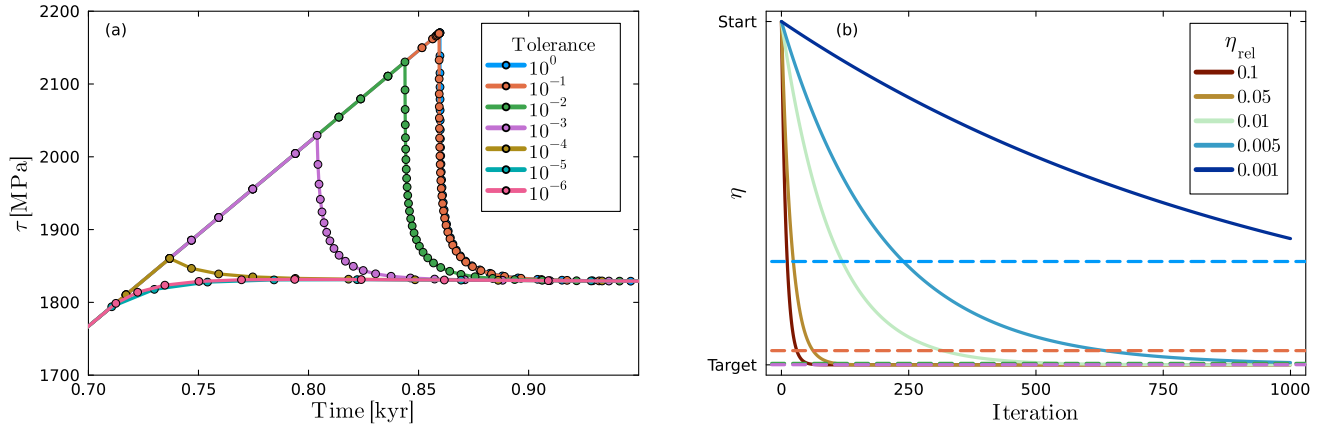


**Figure 7.** Effects of viscosity relaxation. (a) Zoom on transition from elastic loading to LTP in temporal evolution of stress ( $\tau$ ) for different numerical tolerances regarding viscosity relaxation. The stress peak disappears if the tolerance is reduced to  $\sim 10^{-5}$ . (b) Viscosity convergence towards a new value during the PT iterations according to Eq. 26 for different  $\eta_{rel}$ . This evolution is independent of the start and target values. Dashed lines correspond to the tolerances in (a). As all low-tolerance lines overlap, we did not display  $10^{-6}$  to  $10^{-4}$ . The y-axis is logarithmic.

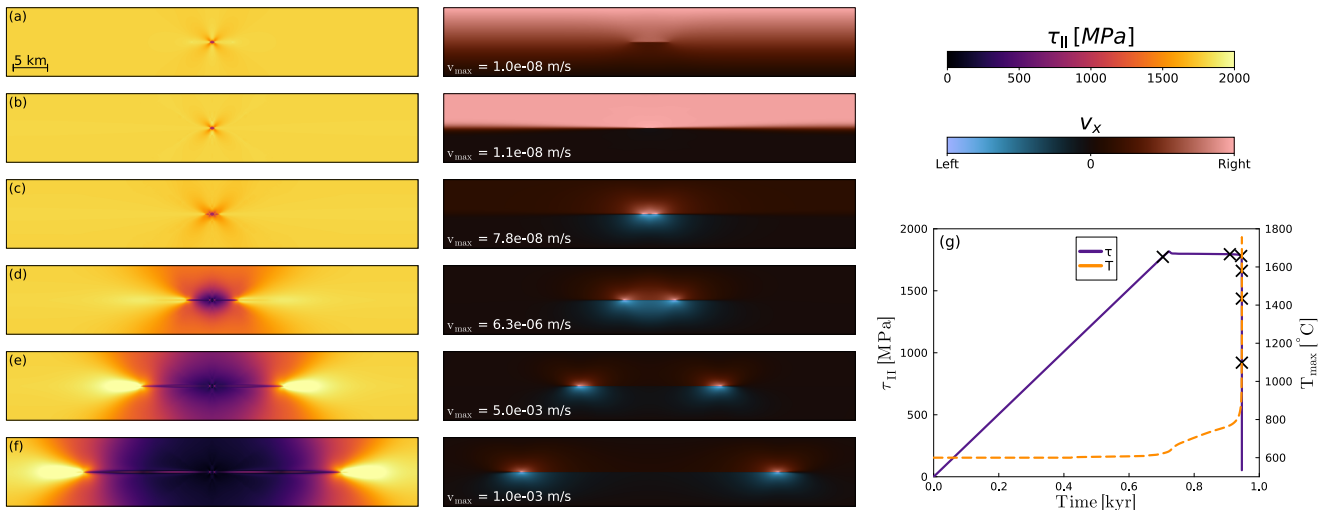


**Figure 8.** Thermal runaway in 2D. (a-f) Temporal evolution of deviatoric stress (left) and horizontal velocity (center) fields. (g) Temporal evolution of average deviatoric stress and maximum temperature. Black crosses along stress curve indicate the six snapshots shown in (a-f).

365 Physically, the key difference from the 1D setup is that thermal runaway occurs in two distinct regions, each propagating through previously intact host rock. In contrast, the 1D model localizes and releases all the energy at a single location within the inclusion. Numerically, the major distinction is the limited resolution in 2D. While the 1D setup allows for significant



grid refinement, the 2D model is limited to a maximum refinement factor (ratio of largest to smallest cell height) of 2. Higher refinement increases cell aspect ratios, which degrades solver convergence.

370 To remove the impact of grid refinement, we ran a 1D model using the same limited refinement as in 2D and compared results (Fig. 9). Both models exhibit very similar trends in deviatoric stress, maximum temperature, maximum velocity, and minimum viscosity. As long as the thermal runaway fronts remain more than 10 km away from the domain boundaries (Fig. 8a-f), the 2D and 1D models show nearly identical  $v_{\max}$  and  $T_{\max}$  (Fig. 9b,c). Once the rupture fronts meet due to periodic boundaries,  $v_{\max}$  increases by a factor of  $\sim 3$  and  $T_{\max}$  by  $\sim 250$  °C.

375 The most notable difference is the duration of the LTP-dominated phase, which lasts over 10 kyr in the 1D model but only  $\sim 200$  years in 2D. This discrepancy stems from differences in how the anomaly is defined. In 1D, only the flow laws of diffusion and dislocation creep are weakened. In 2D, the LTP back stress  $\sigma_b$  is also reduced. Reducing  $\sigma_b$  in 1D prevents stresses in the entire model from reaching values above 1 GPa, while omitting this weakening in 2D hampers localization significantly.

380 Adaptive time stepping remains critical in 2D. During elastic loading, time steps are typically on the order of decades; they shrink to months at the onset of thermal runaway, to hours during rupture propagation, and to seconds at peak velocities. Setting a lower time step bound can dampen thermal runaway, or, if set too high, cause solver failure. For most of the simulations, the predictive time stepping strategy (Sect. 4.1.1) suffices. However, when rupture fronts meet across the periodic boundaries, restarting time steps (Sect. 4.1.3) is required to maintain stability.

385 Regularization plays a similar role in 2D as in 1D. It enforces a lower bound on viscosity and upper bounds on strain rate and velocity. Due to the more limited spatial resolution in 2D, the shear zone thickness is often constrained by grid size unless a high regularization viscosity ( $\approx 10^{16}$  Pa·s) is used. If a higher spatial resolution can be achieved through improved refinement or significant increase in grid cells, regularization viscosity will again become the controlling factor. This equally applies to adaptive rescaling (Sect. 4.2), which becomes essential when smaller time steps and higher velocities exacerbate round-off errors.

390 Finally, monitoring the convergence of the relaxed viscosity (Sect. 4.4) has minimal impact in 2D. Even before reaching the LTP threshold, the number of iterations per time step increases to  $\sim 5000$  to solve the conservation equations, ensuring that the relaxation-based updates are well-converged.

## 6 Conclusions

395 Resolving strain localization owing to thermal runaway represents a numerical challenge due to its spontaneous onset, rapid self-acceleration, extreme localization, and strong gradients in temperature and viscosity. We address these by implementing adaptive time stepping based on changes in stress and temperature and allowing time steps to be restarted if necessary. We achieve a time step reduction by more than ten orders of magnitude without destabilizing the solver. To maintain numerical precision during such extreme changes, we rescale time-dependent properties using an adaptive internal time scale.

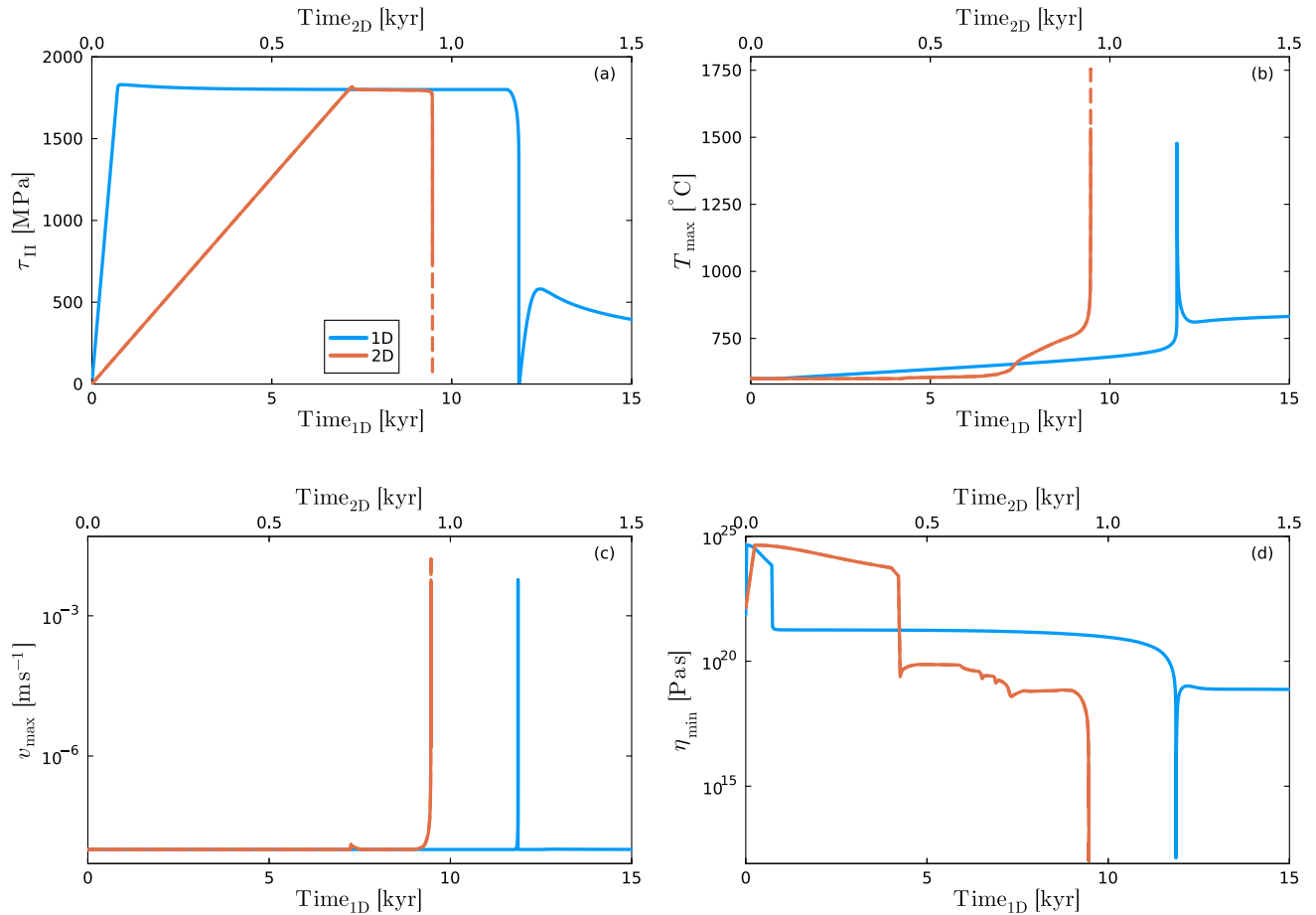


**Figure 9.** Comparison between 1D (blue) and 2D (orange) simulations. Note the different x-axes. Dashed lines indicate the portion of the 2D model influenced by periodic boundary conditions. (a) Mean deviatoric stress. (b) Maximum temperature. (c) Maximum velocity. (d) Minimum viscosity.

400 To handle the self-localizing nature of thermal runaway and prevent solver failure from excessive viscosity reduction, we introduce regularization. Viscosity and gradient regularization both limit maximum velocity and temperature and impose a minimum shear zone width, without altering the overall stress evolution. Viscosity regularization more strongly constrains velocity, whereas gradient regularization better controls temperature increase and shear zone width.

We also show that the commonly used viscosity relaxation method in pseudo-transient schemes can result in incorrect stress  
405 evolutions near the LTP threshold. Only accepting solutions with a sufficiently converged viscosity ensures accurate stress evolution.

Extending the model to two spatial dimensions preserves the key physical behavior observed in 1D. Although 2D simulations are more limited in spatial resolution due to grid aspect ratio constraints, adaptive time stepping, regularization, and rescaling



remain essential. Since 2D models naturally require more iterations per time step, monitoring viscosity convergence is less  
410 critical.

*Code and data availability.* The current version of DEDLoc (Deep Earthquake Ductile Localization) is available from the project website <https://github.com/ArneSpang/DEDLoc> under MIT licence. The exact version of the model used to produce the results of the current study is archived on Zenodo under <https://doi.org/10.5281/zenodo.15481112> (Spang et al., 2025b), as are input data and scripts to run the models for all simulations presented here.

415 *Video supplement.* A video of the 2D model is available on Zenodo under <https://doi.org/10.5281/zenodo.15481112> (Spang et al., 2025b).

## Appendix A: Strain rate partitioning

The solver consists of 6 repeating steps:

1. Compute full strain rate from velocity field
2. Partition strain rate among elasticity, diffusion creep, dislocation creep, low-temperature plasticity, and the regularization
- 420 3. Compute the viscosity of each individual mechanism
4. Compute effective viscosity
5. Compute stress
6. Update velocity, pressure, and temperature

Step 2 is especially challenging, so we present our strategy here. Figure A1 illustrates our rheological model including  
425 viscosity regularization. The main challenges are the partition of stress between the regularization branch (orange in Fig. A1) and the viscous branch (blue in Fig. A1), as well as the partition of the viscous strain rate between the different mechanisms. Stress is equal in sequential components and partitioned in parallel components, strain rate vice-versa (Maxwell, 1867; Józwiak et al., 2015). For clarity, we have neglected the subscript  $\text{II}$  in the following equations.

First, we partition the strain rate between the elastic and viscous / regularization components. The elastic strain rate can be  
430 expressed as follows:

$$\dot{\epsilon}_{\text{el}} = \frac{\tau - \tau^{\text{old}}}{2G\Delta t}, \quad (\text{A1})$$

where  $\tau$  refers to the current stress and old refers to the stress at the end of the previous physical time step. This allows us to compute the viscous strain rate:



$$\dot{\epsilon}_{vi} = \dot{\epsilon} - \dot{\epsilon}_{el}. \quad (A2)$$

435  $\dot{\epsilon}_{vi}$  is identical in the viscous branch and the regularization branch, and since  $\eta_{reg}$  is known, we can express the stress carried by the regularization as follows:

$$\tau_{reg} = 2\dot{\epsilon}_{vi}\eta_{reg}. \quad (A3)$$

As stress is partitioned between the viscous and regularization branch, we can compute the viscous stress by:

$$\tau_{vi} = \tau - \tau_{reg}. \quad (A4)$$

440 Viscous stress is identical in all viscous components, but viscous strain rate is partitioned between them. As diffusion creep viscosity is independent of the partitioning, the diffusion creep component can be computed by:

$$\dot{\epsilon}_{dif} = \frac{\tau_{vi}}{2\eta_{dif}}. \quad (A5)$$

$\dot{\epsilon}_{dif}$  can be subtracted from the viscous strain rate to find the nonlinear part which partitions into dislocation creep and low-temperature plasticity.

$$445 \quad \dot{\epsilon}_{nl} = \dot{\epsilon}_{vi} - \dot{\epsilon}_{dif} = \dot{\epsilon}_{dis} + \dot{\epsilon}_{LTP}. \quad (A6)$$

If neither dislocation creep nor LTP are currently active (i.e. taking a significant strain rate partition),  $\dot{\epsilon}_{nl}$  can become negative. In this case, we overwrite it with a very small positive value as a negative value or zero would cause issues in the viscosity calculation.

As  $\eta_{dis}$  and  $\eta_{LTP}$  both depend on the strain rate partitioning, we can not solve for either strain rate component analogously to Eq. (A5). But, since  $\dot{\epsilon}_{dis}$  and  $\dot{\epsilon}_{LTP}$  are inversely proportional to  $\eta_{dis}$  and  $\eta_{LTP}$  respectively, we can guess their ratio from the viscosities of the previous iteration.

$$\frac{\dot{\epsilon}_{dis}}{\dot{\epsilon}_{LTP}} \approx \frac{\eta_{LTP}^{prev}}{\eta_{dis}^{prev}} = r_{\eta} \quad (A7)$$

This yields:

$$\dot{\epsilon}_{dis,g} = \dot{\epsilon}_{nl} \frac{r_{\eta}}{1 + r_{\eta}}, \quad (A8)$$

$$455 \quad \dot{\epsilon}_{LTP,g} = \dot{\epsilon}_{nl} \frac{1}{1 + r_{\eta}}, \quad (A9)$$



where  $\dot{\epsilon}_{\text{dis},g}$  and  $\dot{\epsilon}_{\text{LTP},g}$  are guesses for the strain rate of dislocation creep and low-temperature plasticity respectively.  $\eta_{\text{dis}}$  and  $\eta_{\text{LTP}}$  are computed with these guesses according to Eq. (22) and (23), and after stress has been updated, the true partitioning for both mechanisms can be computed analogously to Eq. (A5):

$$\dot{\epsilon}_{\text{dis}} = \frac{\tau_{\text{vi}}}{2\eta_{\text{dis}}}, \quad (\text{A10})$$

$$460 \quad \dot{\epsilon}_{\text{LTP}} = \frac{\tau_{\text{vi}}}{2\eta_{\text{LTP}}}. \quad (\text{A11})$$

During the pseudo-time iterations,  $\dot{\epsilon}_{\text{dis},g}$  and  $\dot{\epsilon}_{\text{LTP},g}$  converge towards  $\dot{\epsilon}_{\text{dis}}$  and  $\dot{\epsilon}_{\text{LTP}}$  respectively. We track this convergence and use it as an additional requirement for a solution to be accepted. If gradient regularization is used, the orange component in Fig. A1 is missing, and  $\tau_{\text{vi}} = \tau$ .

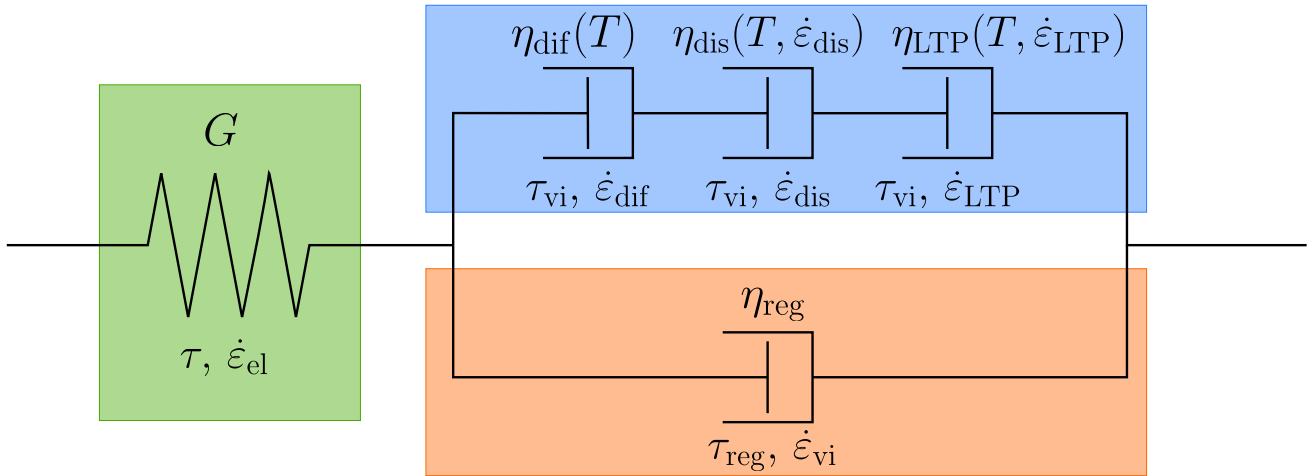


**Figure A1.** Illustration of our rheological model including the viscous regularization. Green shaded region shows elastic component, blue shows viscous component, and orange shows regularization component. Individual deformation mechanisms are labeled with their respective stresses and strain rates.

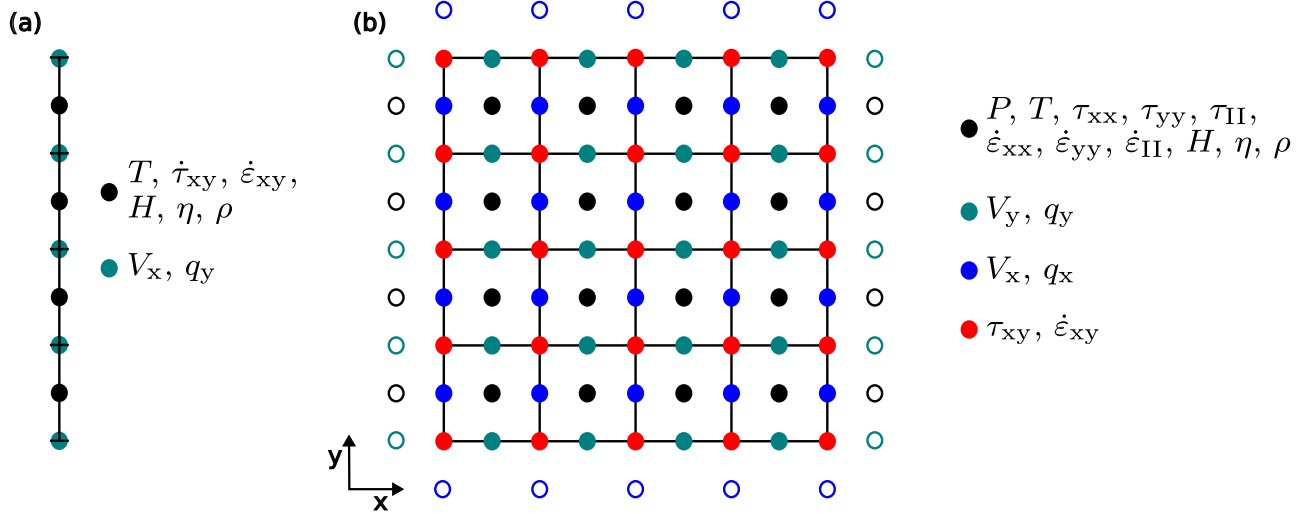


**Figure A2.** Illustration of staggered numerical grid, indicating where different parameters are computed. (a) 1D. (b) 2D. Hollow circles are ghost nodes outside the physical domain which are necessary to employ boundary conditions. Modified from Spang et al. (2025a).

*Author contributions.* AS was the main developer of the code and methodology of the study, ran all simulations, processed the results, produced the Figures, wrote the original manuscript and edited it after co-author revision. MT contributed to the methodology, provided the funding and reviewed the manuscript. CP provided the theory for the gradient regularization. AdM and LR helped with the implementation of the pseudo-transient method, reviewed and edited the manuscript.

*Competing interests.* The authors have no competing interests to declare.

*Acknowledgements.* A.S. and M.T. were funded by the DFG grant TH 2076/8-1 awarded to M.T.. This research has been supported by the Swiss University Conference and the Swiss Council of Federal Institutes of Technology through the Platform for Advanced Scientific Computing (PASC), obtained via the PASC project GPU4GEO.





## References

- Alkhimenkov, Y. and Podladchikov, Y. Y.: Accelerated pseudo-transient method for elastic, viscoelastic, and coupled hydro-mechanical problems with applications, *Geoscientific Model Development Discussions*, 2024, 1–35, <https://doi.org/https://doi.org/10.5194/gmd-18-563-2025>, 2024.
- Alkhimenkov, Y., Khakimova, L., Utkin, I., and Podladchikov, Y.: Resolving strain localization in frictional and time-dependent plasticity: Two-and three-dimensional numerical modeling study using graphical processing units (GPUs), *Journal of Geophysical Research: Solid Earth*, 129, e2023JB028566, <https://doi.org/https://doi.org/10.1029/2023JB028566>, 2024.
- Antolovich, S. D. and Armstrong, R. W.: Plastic strain localization in metals: origins and consequences, *Progress in Materials Science*, 59, 1–160, <https://doi.org/https://doi.org/10.1016/j.pmatsci.2013.06.001>, 2014.
- Braeck, S., Podladchikov, Y. Y., and Medvedev, S.: Spontaneous dissipation of elastic energy by self-localizing thermal runaway, *Physical Review E*, 80, 046105, <https://doi.org/https://doi.org/10.1103/PhysRevE.80.046105>, 2009.
- Byerlee, J.: Friction of rocks, in: *Rock friction and earthquake prediction*, pp. 615–626, Birkhäuser, Basel, <https://doi.org/https://doi.org/10.1007/978-3-0348-7182-2>, 1978.
- Dal Zilio, L., Hegyi, B., Behr, W., and Gerya, T.: Hydro-mechanical earthquake cycles in a poro-visco-elasto-plastic fluid-bearing fault structure, *Tectonophysics*, 838, 229–251, <https://doi.org/https://doi.org/10.1016/j.tecto.2022.229516>, 2022.
- De Borst, R. and Mühlhaus, H.-B.: Gradient-dependent plasticity: formulation and algorithmic aspects, *International journal for numerical methods in engineering*, 35, 521–539, <https://doi.org/https://doi.org/10.1002/nme.1620350307>, 1992.
- De Borst, R., Sluys, L. J., Mühlhaus, H.-B., and Pamin, J.: Fundamental issues in finite element analyses of localization of deformation, *Engineering computations*, 10, 99–121, <https://doi.org/https://doi.org/10.1108/eb023897>, 1993.
- Desrues, J., Bésuelle, P., and Lewis, H.: Strain localization in geomaterials, <https://doi.org/https://doi.org/10.1144/SP289.4>, 2007.
- Drucker, D. C. and Prager, W.: Soil mechanics and plastic analysis or limit design, *Quarterly of applied mathematics*, 10, 157–165, 1952.
- Duretz, T., Räss, L., Podladchikov, Y., and Schmalholz, S.: Resolving thermomechanical coupling in two and three dimensions: spontaneous strain localization owing to shear heating, *Geophysical Journal International*, 216, 365–379, <https://doi.org/https://doi.org/10.1093/gji/ggy434>, 2019.
- Duretz, T., de Borst, R., Yamato, P., and Le Pourhiet, L.: Toward robust and predictive geodynamic modeling: The way forward in frictional plasticity, *Geophysical Research Letters*, 47, e2019GL086027, <https://doi.org/https://doi.org/10.1029/2019GL086027>, 2020.
- Duretz, T., Räss, L., de Borst, R., and Hageman, T.: A comparison of plasticity regularization approaches for geodynamic modeling, *Geochemistry, Geophysics, Geosystems*, 24, e2022GC010675, <https://doi.org/https://doi.org/10.1029/2022GC010675>, 2023.
- Frankel, S. P.: Convergence rates of iterative treatments of partial differential equations, *Mathematics of Computation*, 4, 65–75, 1950.
- Gerolymatou, E., Stathas, A., and Stefanou, I.: Do multiphysics processes lead to mesh independent analyses?, *International Journal of Mechanical Sciences*, 274, 109265, <https://doi.org/https://doi.org/10.1016/j.ijmecsci.2024.109265>, 2024.
- Gerya, T. V.: *Introduction to numerical geodynamic modelling*, Cambridge University Press, 2019.
- Gerya, T. V. and Yuen, D. A.: Characteristics-based marker-in-cell method with conservative finite-differences schemes for modeling geological flows with strongly variable transport properties, *Physics of the Earth and Planetary Interiors*, 140, 293–318, <https://doi.org/https://doi.org/10.1016/j.pepi.2003.09.006>, 2003.
- Goudarzi, M., Gerya, T., and Dinther, Y. v.: A comparative analysis of continuum plasticity, viscoplasticity and phase-field models for earthquake sequence modeling, *Computational Mechanics*, 72, 615–633, <https://doi.org/https://doi.org/10.1007/s00466-023-02311-0>, 2023.



- Gruntfest, I.: Thermal feedback in liquid flow; plane shear at constant stress, *Transactions of the Society of Rheology*, 7, 195–207, <https://doi.org/https://doi.org/10.1122/1.548954>, 1963.
- Hansen, L. N., Kumamoto, K. M., Thom, C. A., Wallis, D., Durham, W. B., Goldsby, D. L., Breithaupt, T., Meyers, C. D., and Kohlstedt, D. L.: Low-temperature plasticity in olivine: Grain size, strain hardening, and the strength of the lithosphere, *Journal of Geophysical Research: Solid Earth*, 124, 5427–5449, <https://doi.org/https://doi.org/10.1029/2018JB016736>, 2019.
- Herrendörfer, R., Gerya, T., and van Dinther, Y.: An invariant rate-and state-dependent friction formulation for viscoelastoplastic earthquake cycle simulations, *Journal of Geophysical Research: Solid Earth*, 123, 5018–5051, <https://doi.org/https://doi.org/10.1029/2017JB015225>, 2018.
- Hirth, G. and Kohlstedt, D. L.: Rheology of the upper mantle and the mantle wedge: A view from the experimentalists, *Geophysical monograph-american geophysical union*, 138, 83–106, 2003.
- Iordache, M.-M. and Willam, K.: Localized failure analysis in elastoplastic Cosserat continua, *Computer Methods in Applied Mechanics and Engineering*, 151, 559–586, [https://doi.org/https://doi.org/10.1016/S0045-7825\(97\)00166-7](https://doi.org/https://doi.org/10.1016/S0045-7825(97)00166-7), 1998.
- Jacquey, A. B. and Cacace, M.: Multiphysics modeling of a brittle-ductile lithosphere: 1. Explicit visco-elasto-plastic formulation and its numerical implementation, *Journal of Geophysical Research: Solid Earth*, 125, e2019JB018474, <https://doi.org/https://doi.org/10.1029/2019JB018474>, 2020.
- Jacquey, A. B., Rattez, H., and Veveakis, M.: Strain localization regularization and patterns formation in rate-dependent plastic materials with multiphysics coupling, *Journal of the Mechanics and Physics of Solids*, 152, 104422, <https://doi.org/https://doi.org/10.1016/j.jmps.2021.104422>, 2021.
- Jóźwiak, B., Orczykowska, M., and Dziubiński, M.: Fractional generalizations of Maxwell and Kelvin-Voigt models for biopolymer characterization, *PloS one*, 10, e0143090, <https://doi.org/https://doi.org/10.1371/journal.pone.0143090>, 2015.
- Kameyama, M., Yuen, D. A., and Karato, S.-I.: Thermal-mechanical effects of low-temperature plasticity (the Peierls mechanism) on the deformation of a viscoelastic shear zone, *Earth and Planetary Science Letters*, 168, 159–172, [https://doi.org/https://doi.org/10.1016/S0012-821X\(99\)00040-0](https://doi.org/https://doi.org/10.1016/S0012-821X(99)00040-0), 1999.
- Kaus, B. J. P., de Montserrat, A., Medinger, N., Riel, N., Cosarinky, M., Berlie, N., Spang, A., Kiss, D., Ranocha, H., Fuchs, L., Räss, L., Aellig, P., Seiler, A., and Duretz, T.: JuliaGeodynamics/GeoParams.jl: v0.5.1, <https://doi.org/10.5281/zenodo.10050339>, 2023.
- Kelemen, P. B. and Hirth, G.: A periodic shear-heating mechanism for intermediate-depth earthquakes in the mantle, *Nature*, 446, 787–790, <https://doi.org/https://doi.org/10.1038/nature05717>, 2007.
- Kiss, D., Moulas, E., Kaus, B. J. P., and Spang, A.: Decompression and fracturing caused by magmatically induced thermal stresses, *Journal of Geophysical Research: Solid Earth*, 128, e2022JB025341, 2023.
- Leith, A. and Sharpe, J.: Deep-focus earthquakes and their geological significance, *The Journal of Geology*, 44, 877–917, <https://doi.org/https://doi.org/10.1086/624495>, 1936.
- Maxwell, J. C.: IV. On the dynamical theory of gases, *Philosophical transactions of the Royal Society of London*, pp. 49–88, <https://doi.org/https://doi.org/10.1098/rstl.1867.0004>, 1867.
- Ogawa, M.: Shear instability in a viscoelastic material as the cause of deep focus earthquakes, *Journal of Geophysical Research: Solid Earth*, 92, 13 801–13 810, <https://doi.org/https://doi.org/10.1029/JB092iB13p13801>, 1987.
- Omlin, S. and Räss, L.: High-performance xPU Stencil Computations in Julia, *Proceedings of the JuliaCon Conferences*, 6, 138, <https://doi.org/10.21105/jcon.00138>, 2024.



- Poirier, J.: Shear localization and shear instability in materials in the ductile field, *Journal of Structural Geology*, 2, 135–142, [https://doi.org/https://doi.org/10.1016/0191-8141\(80\)90043-7](https://doi.org/https://doi.org/10.1016/0191-8141(80)90043-7), 1980.
- Pranger, C., Sanan, P., May, D. A., Le Pourhiet, L., and Gabriel, A.-A.: Rate and state friction as a spatially regularized transient viscous flow law, *Journal of Geophysical Research: Solid Earth*, 127, e2021JB023 511, <https://doi.org/https://doi.org/10.1029/2021JB023511>, 2022.
- 550 Räss, L., Utkin, I., Duretz, T., Omlin, S., and Podladchikov, Y. Y.: Assessing the robustness and scalability of the accelerated pseudo-transient method, *Geoscientific Model Development*, 15, 5757–5786, <https://doi.org/https://doi.org/10.5194/gmd-15-5757-2022>, 2022.
- Ropp, D. L., Shadid, J. N., and Ober, C. C.: Studies of the accuracy of time integration methods for reaction–diffusion equations, *Journal of computational physics*, 194, 544–574, <https://doi.org/https://doi.org/10.1016/j.jcp.2003.08.033>, 2004.
- Sleep, N. H.: Application of a unified rate and state friction theory to the mechanics of fault zones with strain localization, *Journal of*
- 555 *Geophysical Research: Solid Earth*, 102, 2875–2895, <https://doi.org/https://doi.org/10.1029/96JB03410>, 1997.
- Spang, A., Thielmann, M., and Kiss, D.: Rapid ductile strain localization due to thermal runaway, *Journal of Geophysical Research: Solid Earth*, 129, e2024JB028 846, <https://doi.org/https://doi.org/10.1029/2024JB028846>, 2024.
- Spang, A., Thielmann, M., de Montserrat Navarro, A., and Duretz, T.: Transient propagation of ductile ruptures by thermal runaway, *Authorea Preprints*, <https://doi.org/10.22541/essoar.173884466.65638309/v1>, 2025a.
- 560 Spang, A., Thielmann, M., Pranger, C., de Montserrat, A., and Räss, L. G.: Numerical model used in "Overcoming the numerical challenges owing to rapid ductile localization" , <https://doi.org/10.5281/zenodo.15481112>, 2025b.
- Thielmann, M.: Grain size assisted thermal runaway as a nucleation mechanism for continental mantle earthquakes: Impact of complex rheologies, *Tectonophysics*, 746, 611–623, <https://doi.org/https://doi.org/10.1016/j.tecto.2017.08.038>, 2018.
- Thielmann, M., Rozel, A., Kaus, B. J. P., and Ricard, Y.: Intermediate-depth earthquake generation and shear zone formation caused by grain
- 565 size reduction and shear heating, *Geology*, 43, 791–794, <https://doi.org/https://doi.org/10.1130/G36864.1>, 2015.
- Turner, H.: On the Arrival of Earthquake Waves at the Antipodes, and on the Measurement of the Focal Depth of an Earthquake., *Geophysical journal international*, 1, 1–13, <https://doi.org/https://doi.org/10.1111/j.1365-246X.1922.tb05354.x>, 1922.
- Wadati, K.: Shallow and deep earthquakes, *Geophys. Mag.*, 1, 162–202, 1928.
- Weidner, A. and Biermann, H.: Review on strain localization phenomena studied by high-resolution digital image correlation, *Advanced*
- 570 *Engineering Materials*, 23, 2001 409, <https://doi.org/https://doi.org/10.1002/adem.202001409>, 2021.